Physical Properties of RhGe and CoGe Single Crystals Synthesized under High Pressure

Shangjie Tian(田尚杰)[1,2,3†], Xiangjiang Dong(董祥江)[4†], Bowen Zhang(张博文)[4], Zhijun Tu(涂志俊)[2,3], Runze Yu(于润泽)[4*], Hechang Lei(雷和畅)[2,3*], and Shouguo Wang(王守国)[1*]

[1]*Anhui Provincial Key Laboratory of Magnetic Functional Materials and Devices, School of Materials Science and Engineering, Anhui University, Hefei 230601, China*
[2]*School of Physics and Beijing Key Laboratory of Optoelectronic Functional Materials & MicroNano Devices, Renmin University of China, Beijing 100872, China*
[3]*Key Laboratory of Quantum State Construction and Manipulation (Ministry of Education), Renmin University of China, Beijing 100872, China*
[4]*Center for High-Pressure Science and Technology Advanced Research, Beijing 100193, China*

(Received 6 August 2025; accepted manuscript online 26 September 2025)

Chiral topological semimetals hosting multifold fermions and exotic surface states represent a frontier in topological materials research. Among them, noncentrosymmetric cubic B20 compounds—notably transition-metal silicides and germanides—offer a unique platform for realizing symmetry-protected topological phases and unconventional optoelectronic responses. Here, we report the physical properties of RhGe and CoGe single crystals with B20 structure in detail. Transport measurements revea metallic behavior with characteristic Fermi-liquid scaling at low temperatures, while magnetization results confirm paramagnetism in both compounds. In addition, both materials exhibit low carrier concentrations with small electronic specific heat coefficients, indicating their semimetal feature with weak electronic correlations. Such high-quality CoGe and RhGe single crystals provide a material platform to explore the evolution of multifold fermions and the instability of helicoid-arc surface states with spin–orbit coupling and surface environment in B20 material systems.

DOI: 10.1088/0256-307X/42/11/110708 CSTR: 32039.14.0256-307X.42.11.110708

1. Introduction. The existence of nontrivial band topology generates exotic quantum phenomena in condensed matter physics, establishing topological materials as a major research frontier since the discovery of topological insulators and semimetals.[1–6] Fundamental fermionic particles predicted in high-energy physics—including Dirac, Weyl, and Majorana fermions—emerge as low-energy quasiparticle excitations within these materials. Dirac semimetals host four-fold degenerate nodes exhibiting linear dispersion in all momentum directions, protected by combined inversion, time-reversal, and lattice symmetries.[7–9] Breaking either inversion or time-reversal symmetry splits Dirac nodes into Weyl points (characterized by a Chern number $|C| = 1$), generating distinctive Fermi arc surface states (SSs).[10,11] Chirality, degeneracy, and dimensionality further define diverse topological phases,[12–15] while non-symmorphic symmetries enforce high-symmetry-point band crossings that produce higher-fold fermions. Recent advances reveal massless fermions beyond standard model analogues, such as spin-1 chiral fermions, double Weyl fermions, and spin-3/2 Rarita–Schwinger–Weyl fermions, characterized by higher quantized Chern numbers.[16–19]

Transition metal monosilicides and monogermanides crystallizing in the cubic noncentrosymmetric B20 structure (space group $P2_13$, No. 198) exhibit a rich spectrum of magnetic, topological, and transport properties.[20–38] The inherent structural chirality in these materials dictates both electronic and magnetic behaviors, leading to some unusual phenomena in real and reciprocal spaces. On the one hand, structural chirality induces a finite spin-orbit-driven Dzyaloshinskii–Moriya interaction, which competes with the Heisenberg exchange coupling. This competition underpins unusual magnetic properties, including the observation of skyrmion phases in compounds such as MnSi, FeGe, MnGe, and solid solutions like $Fe_{1-x}Co_xSi$ and $Fe_{1-x}Mn_xSi$.[20,21] On the other hand, in nonmagnetic B20 systems, structural chirality enables chiral topological semimetal states. These states host non-symmorphic symmetry-protected multifold fermions at high-symmetry points.[19,22–27] For example, when neglecting spin–orbit coupling (SOC), the band structures of CoSi exhibit a threefold degenerate crossing (spin-1 fermion) at the Γ point and a four-fold degenerate crossing (double Weyl fermion) at the R point, carrying chiral charges of $+2$ and -2 respectively.[22–24] Such unconventional quasiparticles can give rise to novel optoelectronic responses, such as circular photogalvanic effect.[28,29] The SSs of CoSi and RhSi

†These authors contributed equally to this work.
*Corresponding authors. Email: runze.yu@hpstar.ac.cn; hlei@ruc.edu.cn; sgwang@ahu.edu.cn
© 2025 Chinese Physical Society and IOP Publishing Ltd. All rights, including for text and data mining, AI training, and similar technologies, are reserved.

also demonstrate long Fermi arcs but they possess two different types of helicoid arc van Hove singularities,[30,31] indicating the diversity of SSs due to distinct chemical environments of the surface and SOC. Furthermore, theoretical studies have recently substantiated the potential for topological superconductivity in B20-structured RhGe.[32]

Despite their intriguing topological properties, the studies on B20 RhGe and CoGe, which are isoelectronic to RhSi and CoSi, remain scarce and controversial due to the significant challenges associated with their single-crystal synthesis, which necessitates high-pressure and high-temperature conditions.[33–36] Previous study of RhGe polycrystal suggested there is a coexistence of weak itinerant ferromagnetism ($T_C \sim 140$ K) and superconductivity ($T_c \sim 4.3$ K) in this material,[35] but our preliminary experimental results on RhGe single crystals indicate that both behaviors are absent.[37] In contrast, CoGe exhibits Pauli paramagnetism.[39,40] In this work, we study the physical properties of CoGe and RhGe single crystals grown by using high-pressure and high-temperature methods. Both materials exhibit paramagnetic metallic behaviors with low concentrations of electron-type charge carriers.

2. Methods. Single crystals of RhGe and CoGe were grown under high pressure in a cubic anvil apparatus. High-purity elemental precursors (Rh: 99.99%, Co: 99.95% and Ge: 99.99%) were homogenized by grinding with stoichiometric ratios of Rh:Ge = 1:1.2 (excess Ge serving as solvent flux) and Co:Ge = 1:1, respectively, sealed in hBN capsules (Au and Pt capsules were avoided because they can react with Ge under high temperature and high pressure). They were then positioned at the center of the high-pressure cell and compressed to 5 GPa. For RhGe (CoGe), the temperature was ramped to 1250 ℃ (1100 ℃) at 10 ℃/min, maintained for 3 h (2 h), slowly cooled to 800 ℃ (700 ℃), and finally quenched to ambient temperature prior to decompression.

The powder X-ray diffraction (PXRD) patterns of crushed RhGe and CoGe crystals were performed using a high-resolution diffractometer (Bruker D8) with Cu K_α radiation ($\lambda = 1.5406$ Å) at room temperature. The single-crystal orientations of RhGe and CoGe were determined using a Laue method in backscattering mode (SmartLab, Rigaku). Scanning electron microscopy imaging and energy-dispersive X-ray (EDX) spectroscopy for chemical composition analysis were performed using a JEOL JSM-7000F field-emission scanning electron microscope. Electrical transport measurements were conducted using a superconducting magnetic system (Cryomagnetics, C-Mag Vari-9). Magnetization and heat capacity measurements were performed using a Quantum Design magnetic property measurement system (MPMS3) and physical property measurement system (PPMS-14T), respectively.

3. Results and Discussions. The RhGe and CoGe compounds crystallize in the non-centrosymmetric cubic chiral B20 structure (space group $P2_13$, No. 198),[22,33–35,40] isostructural to CoSi.[23,24] This non-symmorphic chiral framework features a distorted rocksalt-type arrangement with atomic displacements along the [111] direction [Fig. 1(a)]. Figures 1(b) and 1(c) display the PXRD patterns for both compounds measured at room temperature and ambient pressure, accompanied by Rietveld refinement profiles, confirming the phase-pure B20 structures. The refinement parameters (R_{wR} = 7.504% for RhGe and 1.046% for CoGe) demonstrate high model reliability.

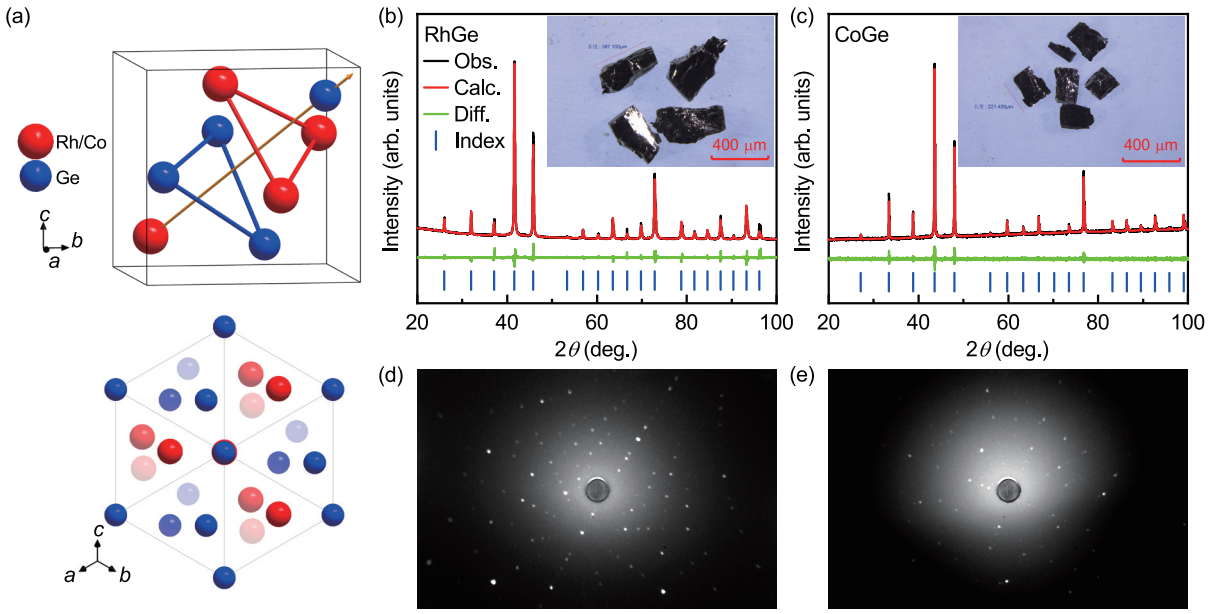

Fig. 1. (a) The B20 cubic crystal structure of RhGe and CoGe with origin shift $(0.23, 0.23, 0.23)$. The blue and red balls represent Rh/Co and Ge atoms, respectively. The orange arrow in the upper panel indexes the [111] direction. The helix arrangements are clearly visible in the top view along the [111]-direction (lower panel). PXRD patterns of (b) RhGe and (c) CoGe along with the Rietveld refinements are shown. The insets show photographs of each single crystal. Laue diffraction patterns of (d) RhGe and (e) CoGe single crystals.

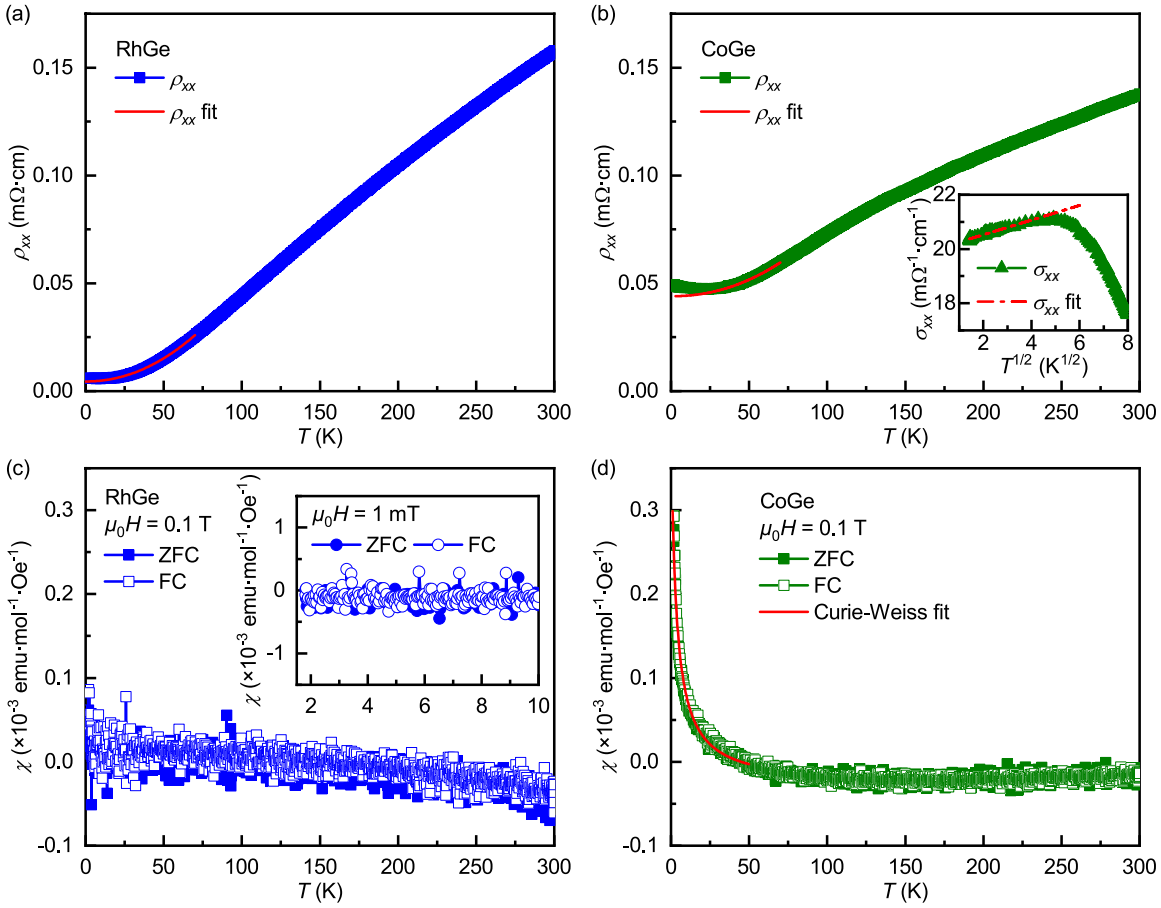

Fig. 2. Temperature dependence of $\rho_{xx}(T)$ of (a) RhGe and (b) CoGe single crystals. The red solid lines show the fits using the formula $\rho_{xx}(T) = \rho_0 + AT^n$. The inset of (b) shows longitudinal conductivity σ_{xx} as a function of $T^{1/2}$ for CoGe single crystals, accompanied by a linear fit. The temperature dependence of $\chi(T)$ at a field of 0.1 T with ZFC and FC modes for (c) RhGe and (d) CoGe single crystal, respectively. The inset of (c) shows $\chi(T)$ data at $\mu_0 H = 1$ mT with ZFC mode. The red lines in (d) show the fits using the modified Curie–Weiss law $\chi = \chi_0 + C/(T - T_\theta)$.

The fitted a-axial lattice parameter is 0.4859(2) nm and 0.4640(1) nm for RhGe and CoGe, respectively, which are in agreement with the reported values in literature for polycrystalline samples.[33,35,39–41] The larger lattice constant of RhGe than that of CoGe can be ascribed to the larger ionic radius of Rh than Co. The B20 structure contains eight atoms per unit cell with Rh/Co and Ge occupying Wyckoff positions 4a at fractional coordinates: (u, u, u), $(u + 0.5, 0.5 - u, -u)$, $(u, 0.5 + u, 0.5 - u)$, and $(0.5 - u, u, 0.5 + u)$. The refined positional parameter u is 0.1086(2) for Rh and 0.9023(4) for Ge in RhGe, while CoGe shows $u = 0.135(4)$ for Co and 0.837(2) for Ge. EDX analysis determined the composition to be Rh:Ge = 1.08(1):1 for RhGe, which is close to the ideal stoichiometric ratio. For CoGe, however, the measured ratio of Co:Ge was 1.25(1):1, suggesting the presence of excess Co and related defects. Figures 1(d) and 1(e) present the Laue diffraction patterns of RhGe and CoGe single crystals along the high-symmetry (100) plane, exhibiting sharp, well-indexed diffraction spots with cubic symmetry, further attesting to the high quality and structural integrity of grown single crystals.

The temperature-dependent electrical resistivity $\rho_{xx}(T)$ of RhGe and CoGe single crystals is shown in Figs. 2(a) and 2(b). Both of them exhibit metallic behaviors in general, and the residual resistivity ratios (RRR) are about 27 and 2 for RhGe and CoGe, respectively. For RhGe, $\rho_{xx}(T)$ decreases linearly from $\sim$150 μΩ·cm at 300 K down to $\sim$30 μΩ·cm at temperature $\sim$70 K, indicating the dominant electron–phonon scattering in the high-temperature region. The $\rho_{xx}(T)$ can be fitted using $\rho_{xx}(T) = \rho_0 + AT^n$ between 20–70 K; the obtained n is 2.05(2), implying that Fermi-liquid behavior appears in the low-temperature region of RhGe. It is noted that superconductivity is absent in present RhGe crystals when the temperature is above 1.8 K, consistent with our previous results.[37] As emphasized in Ref. [35], superconductivity in RhGe is highly sensitive to sample composition and applied pressure. The EDX analysis revealed a slight compositional difference between our single crystals and the superconducting polycrystals. We therefore suggest that the absence of superconductivity in our samples may be attributed to these subtle differences in composition and/or residual strain, which can inherently arise from differences in synthesis methods. For CoGe crystal, it displays similar trends to RhGe but with lower resistivity ($\sim$120 μΩ·cm

at 300 K). The $\rho_{xx}(T)$ curve shows a linear behavior with lowering T down to 180 K and changes to a $T^{2.06(4)}$ dependence between 40–70 K, consistent with Fermi-liquid behavior. When $T < 25$ K, a subtle resistivity upturn can be observed. Such low-T resistivity increase is generally attributed to three mechanisms: weak localization (WL), Kondo effect, and electron–electron interaction (EEI), etc. However, WL and the Kondo effect will lead to a negative magnetoresistance (MR) when applying a magnetic field and are safely excluded here due to being inconsistent with the positive MR of CoGe (discussed below).[42–44] As depicted in the inset of Fig. 2(b), the upturn part in conductivity curve follows a $T^{1/2}$ dependence, suggesting the existence of EEI in the presence of disorder.[42] We propose that the disorder may arise from excess Co defects in CoGe.

Temperature dependence of magnetic susceptibility $\chi(T)$ of RhGe and CoGe at $\mu_0 H = 0.1$ T with zero-field cooling (ZFC) and field cooling (FC) modes is shown in Figs. 2(c) and 2(d). For RhGe, the $\chi(T)$ curve exhibits a weak temperature dependence in the whole temperature range [Fig. 2(c)], suggesting a Pauli paramagnetic behavior. In the low-temperature region, the absence of diamagnetic signal in the $\chi(T)$ curve at $\mu_0 H = 1$ mT with ZFC mode [inset of Fig. 2(c)] confirms that there is no superconducting transition in present RhGe single crystals, consistent with resistivity data. For CoGe, the $\chi(T)$ curve shows a similar behavior to RhGe at $T > 50$ K [Fig. 2(d)], implying the same Pauli paramagnetism. This is consistent with prior reports on CoGe polycrystals.[39,40] When $T < 50$ K, however, the $\chi(T)$ curve of CoGe exhibits a slight upturn behavior [Fig. 2(d)], likely due to trace magnetic impurities, spin fluctuations, or weak electronic correlations. The fitted Curie constant is 0.0014(3) emu·K·mol^{-1}·Oe^{-1} using the modified Curie–Weiss law, $\chi(T) = \chi_0 + C/(T - T_\theta)$, corresponding to 0.11(2) μB/f.u. The observed excess Co from EDX analysis suggests that these atoms may act as magnetic impurities. Assuming these magnetic impurities originate from Co element with a magnetic moment of $3.87\mu_B$, the estimated molar content of magnetic impurities is below 2.8(6)%.

Figures 3(a) and 3(b) present the MR of RhGe and CoGe at various temperatures. RhGe exhibits a large positive MR (∼600%) at 2 K, which diminishes rapidly with increasing temperature. Moreover, the MR curve can be fitted well using the formula $\mathrm{MR} = A(\mu_0 H)^n$ with $n = 1.75(2)$. Such nearly parabolic field dependence suggests that there may be multiple bands with different carrier types (electron or hole) near the Fermi level E_F. In contrast, CoGe displays a weak positive MR (< 3%) across the entire measured range (2–300 K, 0–9 T), comparable to those of CoGe polycrystals[40] and CoSi grown via the chemical vapor transport method.[45] The Hall resistivity $\rho_{yx}(\mu_0 H)$ as a function of magnetic field at various temperatures is shown in Figs. 3(c) and 3(d) for both materials. All curves exhibit negative slopes, indicating the dominance of electron-type carriers in the transport properties. By linearly fitting the $\rho_{yx}(\mu_0 H)$ curves in the high-field region (4–9 T) and combining them with zero-field $\rho_{xx}(T)$ data, the temperature dependence of apparent carrier concentration $n_a(T)$ and mobility $\mu(T)$ can be determined based on a single-band model ($R_H = \rho_{yx}(\mu_0 H)/\mu_0 H = 1/n_a e$ and $\rho_{xx} = ne\mu$, where R_H is Hall coefficient and e is elementary charge). As shown in Fig. 3(e), the carrier concentrations of both compounds at 2 K are comparable: $n_a \sim 4.5 \times 10^{20}$ cm^{-3} and 3.5×10^{20} cm^{-3} for RhGe and CoGe, respectively. Moreover, these values of n_a are also close to that in CoSi.[45,46] With increasing temperature T, the n_a of RhGe increases rapidly, reaching a maximum at $T \sim 160$ K, and then starts to decrease gradually. This implies that at high temperatures there may be more thermally activated hole-type carriers mainly from the band at M point in Brillouin zone, which leads to the decrease of n_a. In contrast, CoGe shows a monotonic mild increase of n_a with increasing T. For RhGe, it exhibits a significantly higher mobility ($\mu \sim 2366$ cm^2·V^{-1}·s^{-1}) than that of CoGe ($\mu \sim 359$ cm^2·V^{-1}·s^{-1}) at 2 K [Fig. 3(f)]. At high T, μ of RhGe undergoes a rapid decay to ~ 350 cm^2·V^{-1}·s^{-1} at $T = 50$ K and finally decreases to ~ 25 cm^2·V^{-1}·s^{-1} at 300 K. For CoGe, its μ peaks at ~ 370 cm^2·V^{-1}·s^{-1} near 25 K [inset of Fig. 3(f)] before declining to ~ 47 cm^2·V^{-1}·s^{-1} at 300 K slowly. Such behavior explains the more obvious low-temperature MR of RhGe when compared to CoGe and its rapid suppression with T. It also suggests that the upturn feature of $\rho_{xx}(T)$ for CoGe at $T \sim 25$ K [Fig. 1(c)] originates from the non-monotonic behavior of μ not from the evolution of n_a.

Specific heat measurements of RhGe and CoGe single crystals, shown in Figs. 4(a) and 4(b), reveal their thermodynamic properties across 2–300 K. For the RhGe single crystal, no anomaly (e.g., specific heat jump) is observed at the specific heat $C_p(T)$ curve at 2.6 K [Fig. 4(a)], consistent with the above resistivity and magnetic susceptibility results. This confirms the absence of superconductivity in the present RhGe single crystal. The high-temperature $C_p(T)$ for both compounds approaches the Dulong–Petit limit (∼57 J·mol^{-1}·K^{-1} at 300 K), consistent with the classical value $3NR$ ($N = 2$ atoms per formula unit, $R = 8.314$ J·mol^{-1}·K^{-1}). At low-temperature region, the $C_p(T)$ data can be fitted well using the formula $C_p/T = \gamma + \beta T^2$, where γ represents the electronic specific heat coefficient and β represents the lattice contribution [insets in Figs. 4(a) and 4(b)]. The fitted γ of RhGe is 0.40(1) mJ·mol^{-1}·K^{-2} and $\beta = 0.084(9)$ mJ·mol^{-1}·K^{-4}, yielding a Debye temperature $\Theta_D = 357(6)$ K via $\Theta_D = (12\pi^4 NR/5\beta)^{1/3}$. CoGe shows a comparable value of γ with RhGe [∼0.24(1) mJ·mol^{-1}·K^{-2}] and a larger $\Theta_D = 403(4)$ K, derived from the value of $\beta = 0.059(2)$ mJ·mol^{-1}·K^{-4}. The latter can be explained by the smaller atomic weight of Co than that of Rh. The values of γ in both RhGe and CoGe are similar to that of CoSi ($\gamma \sim 0.5$–1.2 mJ·mol^{-1}·K^{-2}),[47] but much smaller than MnGe ($\gamma = 16$–20 mJ·mol^{-1}·K^{-2})[39,40] and FeGe ($\gamma = 9$ mJ·mol^{-1}·K^{-2})[40] (summarized in Table 1 with other related B20 materials). It demonstrates that

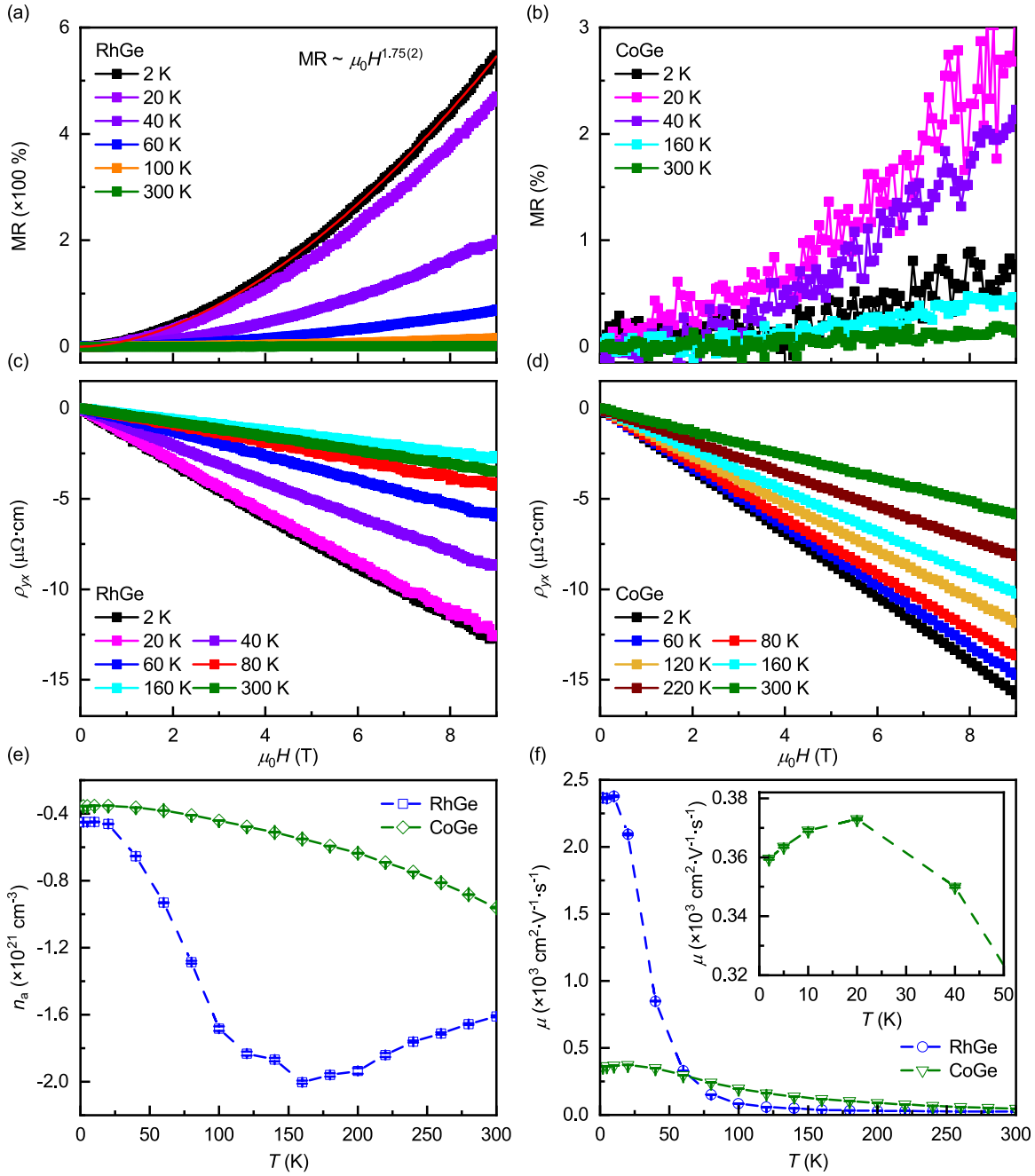

Fig. 3. Field dependence of MR up to $\mu_0 H = 9\,\mathrm{T}$ at various temperatures for (a) RhGe and (b) CoGe single crystals, respectively. The color codes in (a) and (b) are the same. The red solid line in (a) is the fit of MR data at 2 K using $\mathrm{MR} = A(\mu_0 H)^n$. (c) and (d) show the $\rho_{yx}(\mu_0 H)$ of RhGe and CoGe as a function of $\mu_0 H$ between 2 K and 300 K. The color codes in (c) and (d) are the same. (e) Temperature dependences of $n_\mathrm{a}(T)$ for RhGe and CoGe derived from the linear fits of $\rho_{yx}(\mu_0 H)$ curves in the high-field region (4–9 T). (f) Derived temperature dependences of $\mu(T)$ for RhGe and CoGe. Inset: enlarged part of $\mu(T)$ below 50 K for CoGe.

the electron correlations in non-magnetic RhGe, CoGe, and CoSi are weaker than those in magnetic B20 systems.

A comparison of the physical parameters of RhGe and CoGe with other silicide and germanide materials with B20 structure is presented in Table 1. Theoretical calculations indicate that RhGe and CoGe are non-magnetic, and they exhibit remarkably similar electronic band structures, well described within the rigid band approximation framework. States within 5 eV of the Fermi energy (E_F) originate predominantly from transition metal d-orbitals, which are understood to govern many of the intriguing properties in these compounds. Specifically, the Fermi surfaces of CoGe and RhGe comprise electron pockets centered at the Brillouin zone center (Γ point) and corner (R point), alongside a hole pocket at the M point. Additionally, very small hole pockets may exist along the Γ–R direction. All the Fermi surface pockets are rather small and resemble those of semimetals.[19,32,40,48–50] Our magnetic and

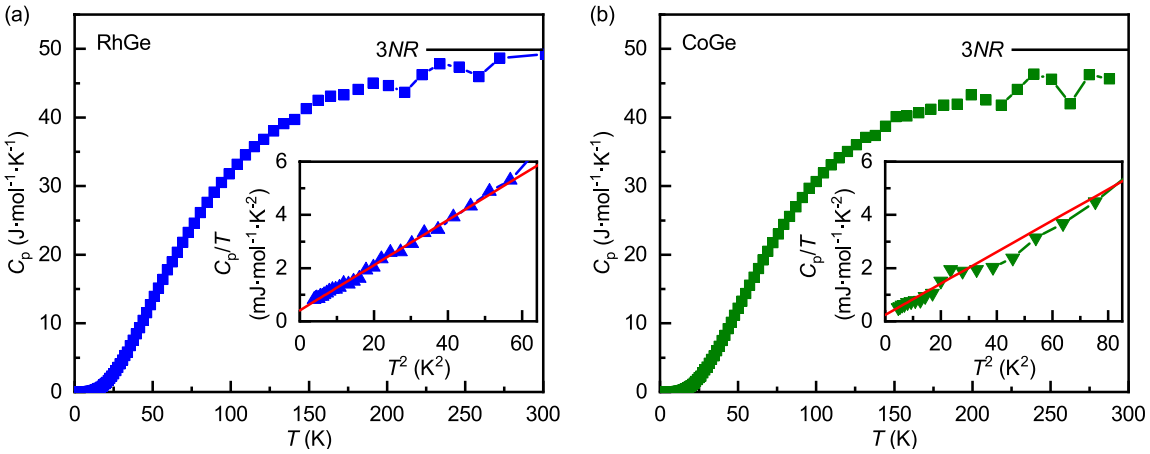

Fig. 4. Temperature dependence of $C_p(T)$ from 2 K to 300 K at zero field for (a) RhGe and (b) CoGe, respectively. Insets of (a) and (b) show the relationship between C_p/T and T^2. The red solid lines represent the fits using the formula $C_p/T = \gamma + \beta T^2$.

Table 1. Summary of physical parameters of some silicide and germanide materials with B20 structure. PM = paramagnetic, UCF = unconventional chiral fermions, SC = superconductivity, HM = helimagnetic, Sky = Skyrmion.

	RRR	MR (%)	n (10^{20} cm^{-3})	μ (cm^2·V^{-1}·s^{-1})	γ (mJ·mol^{-1}·K^{-2})	Properties	Refs.
CoSi	1–30	−1–400	1–3	200–7300	0.5–1.2	PM, UCF	[23,45–47,51]
CoGe	2	< 3	2.5	359	0.24	PM	This work
	1.8	< 0.1	6		0–3	PM, UCF	[39–41,49]
RhSi						PM, UCF	[25,28]
RhGe	27	600	4.5	2366	0.40(1)	PM	This work
	10				2.9	SC ($T_c = 4$ K), UCF	[32,35]
RhSn	24	450	4.6			PM, UCF	[16,52]
FeGe	14	−0.5	2/3 carrier/f.u.		9	HM ($T_C = 280$ K), Sky	[21,40]
MnGe	9.3	< 5	1/2 carrier/f.u.		16–20	HM ($T_C = 275$ K), Sky	[21,39,40]

electrical transport measurements corroborate the theoretical predictions, confirming that both RhGe and CoGe single crystals are paramagnetic metals with low charge carrier density, similar to CoSi. These features likely arise from a significantly reduced density of states at E_F when compared to itinerant ferromagnets like FeGe or MnGe. More importantly, because CoGe and RhGe are isoelectronic to CoSi and RhSi, they should exhibit similar band topology, especially long Fermi arcs. However, different strengths of SOC and subtle surface environments could lead to different connectivity and instability of SSs. Thus, RhGe and CoGe provide a novel platform to study surface-dominant correlation effects in topological semimetals.

4. Conclusions. In summary, we successfully grew high-quality RhGe and CoGe single crystals up to millimeter size under high pressure and high temperature. Transport measurements reveal the metallic behavior of RhGe and CoGe single crystals at low temperatures, while magnetic measurements indicate that both RhGe and CoGe are paramagnets. Neither superconductivity nor ferromagnetism is observed down to 2 K. These high-quality RhGe and CoGe single crystals are a prerequisite for further investigation of their novel topological properties using angle-resolved photoemission spectroscopy (ARPES). Moreover, this study highlights the ongoing challenges of discovering superconductivity in B20-structured materials.

Acknowledgements. This work was supported by National Key R&D Program of China (Grant Nos. 2022-YFA1403800, 2023YFA1406000, and 2023YFA1406500), the National Natural Science Foundation of China (Grant Nos. 12274459, 12474002, 22171283, and 52130103), and China Postdoctoral Science Foundation (Grant No. 2023M730011). This work was supported by the Synergetic Extreme Condition User Facility (SECUF, https://cstr.cn/31123.02.SECUF).

References

[1] Vergniory M, Elcoro L, Felser C, Regnault N, Bernevig B A, and Wang Z 2019 *Nature* **566** 480
[2] Zhang T, Jiang Y, Song Z, Huang H, He Y, Fang Z, Weng H, and Fang C 2019 *Nature* **566** 475
[3] Cano J, Bradlyn B, and Vergniory M 2019 *APL Mater.* **7** 101125
[4] Bradlyn B, Cano J, Wang Z, Vergniory M, Felser C, Cava R J, and Bernevig B A 2016 *Science* **353** aaf5037
[5] Feng X, Zhu J, Wu W, and Yang S A 2021 *Chin. Phys. B* **30** 107304
[6] Li F, Yu T, Lai J, Liu J, Liu P, Chen X Q, and Sun Y 2024 *Chin. Phys. Lett.* **41** 107301
[7] Liu Z, Zhou B, Zhang Y, Wang Z, Weng H, Prabhakaran D, Mo S K, Shen Z, Fang Z, Dai X, Hussain Z, and Chen Y L 2014 *Science* **343** 864

[8] Wang Z, Weng H, Wu Q, Dai X, and Fang Z 2013 *Phys. Rev. B* **88** 125427
[9] Wang J M, Qian H J, Jiang Q, Qiao S, and Ye M 2024 *Chin. Phys. Lett.* **41** 017101
[10] Lv B, Xu N, Weng H, Ma J, Richard P, Huang X, Zhao L, Chen G, Matt C, Bisti F, Strocov V N, Mesot J, Fang Z, Dai X, Qian T, Shi M, and Ding H 2015 *Nat. Phys.* **11** 724
[11] Xu S Y, Belopolski I, Sanchez D S, Zhang C, Chang G, Guo C, Bian G, Yuan Z, Lu H, Chang T R, Shibayev P P, Prokopovych M L, Alidoust N, Zheng H, Lee C C, Huang S M, Sankar R, Chou F, Hsu C H, Jeng H T, Bansil A, Neupert T, Strocov V N, Lin H, Jia S, and Hasan M Z 2015 *Sci. Adv.* **1** e1501092
[12] Chiu C K, Teo J C, Schnyder A P, and Ryu S 2016 *Rev. Mod. Phys.* **88** 035005
[13] Senthil T 2015 *Annu. Rev. Condens. Matter Phys.* **6** 299
[14] Mardanya S, Singh B, Huang S M, Chang T R, Su C, Lin H, Agarwal A, and Bansil A 2019 *Phys. Rev. Mater.* **3** 071201(R)
[15] Zhang A, Deng K, Sheng J, Liu P, Kumar S, Shimada K, Jiang Z, Liu Z, Shen D, Li J, Ren J, Wang L, Zhou L, Ishikawa Y, Ohhara T, Zhang Q, McIntyre M, Yu D, Liu E, Wu L, Chen C, and Liu Q 2023 *Chin. Phys. Lett.* **40** 126101
[16] Li H, Xu S, Rao Z C, Zhou L Q, Wang Z J, Zhou S M, Tian S J, Gao S Y, Li J J, Huang Y B, Lei H C, Weng H M, Sun Y J, Xia T L, Qian T, and Ding H 2019 *Nat. Commun.* **10** 5505
[17] Gao H, Venderbos J W, Kim Y, and Rappe A M 2019 *Annu. Rev. Mater. Res.* **49** 153
[18] Chang G, Wieder B J, Schindler F, Sanchez D S, Belopolski I, Huang S M, Singh B, Wu D, Chang T R, Neupert T, Xu S Y, Lin H, and Hasan M Z 2018 *Nat. Mater.* **17** 978
[19] Tang P, Zhou Q, and Zhang S C 2017 *Phys. Rev. Lett.* **119** 206402
[20] Mulbauer S, Binz B, Jonietz F, Pfleiderer C, Rosch A, Neubauer A, Georgii R, and Böni P 2009 *Science* **323** 915
[21] Tokura Y and Kanazawa N 2021 *Chem. Rev.* **121** 2857
[22] Pshenay-Severin D A and Burkov A T 2019 *Materials* **12** 2710
[23] Rao Z, Li H, Zhang T, Tian S, Li C, Fu B, Tang C, Wang L, Li Z, Fan W, Li J, Huang Y, Liu Z, Long Y, Fang C, Weng H, Shi Y, Lei H, Sun Y, Qian T *et al.* 2019 *Nature* **567** 496
[24] Sanchez D S, Belopolski I, Cochran T A, Xu X, Yin J X, Chang G, Xie W, Manna K, Süß V, Huang C Y, Alidoust N, Multer D, Zhang S S, Shumiya N, Wang X, Wang G Q, Chang T R, Felser C, Xu S Y, Jia S, Lin H, and Hasan M Z 2019 *Nature* **567** 500
[25] Chang G, Xu S Y, Wieder B J, Sanchez D S, Huang S M, Belopolski I, Chang T R, Zhang S, Bansil A, Lin H, and Hasan M Z 2017 *Phys. Rev. Lett.* **119** 206401
[26] Sessi P, Fan F R, Küster F, Manna K, Schröter N B, Ji J R, Stolz S, Krieger J A, Pei D, Kim T K, Dudin P, Cacho C, Widmer R, Borrmann H, Shi W, Chang K, Sun Y, Felser C, and Parkin S S P 2020 *Nat. Commun.* **11** 3507
[27] Yao M, Manna K, Yang Q, Fedorov A, Voroshnin V, Schwarze B V, Hornung J, Chattopadhyay S, Sun Z, Guin S N, Wosnitza J, Borrmann H, Shekhar C, Kumar N, Fink J, Sun Y, and Felser C 2020 *Nat. Commun.* **11** 20333
[28] Rees D, Manna K, Lu B, Morimoto T, Borrmann H, Felser C, Moore J, Torchinsky D H, and Orenstein J 2020 *Sci. Adv.* **6** eaba0509
[29] Ni Z, Wang K, Zhang Y, Pozo O, Xu B, Han X, Manna K, Paglione J, Felser C, Grushin A G, de Juan F, Mele E J, and Wu L 2021 *Nat. Commun.* **12** 154
[30] Rao Z C, Tian S J, Gao S Y, Hu Q X, Fan W H, Huang J R, Tang C Y, Huang Y B, Lei H C, Sun Y J, Qian T, and Ding H 2022 *Sci. China Phys. Mech. Astron.* **65** 257013
[31] Sanchez D S, Cochran T A, Belopolski I, Cheng Z J, Yang X P, Liu Y, Hou T, Xu X, Manna K, Shekhar C, Yin J X, Borrmann H, Chikina A, Denlinger J D, Strocov V N, Xie W, Felser C, Jia S, Chang G, and Hasan M Z 2023 *Nat. Phys.* **19** 682
[32] Mardanya S, Kargarian M, Verma R, Chang T R, Chowdhury S, Lin H, Bansil A, Agarwal A, and Singh B 2024 *Phys. Rev. Mater.* **8** L091801
[33] Larchev V I and Popova S V 1982 *J. Less-Common Met.* **87** 53
[34] Takizawa H, Sato T, Endo T, and Shimada M 1988 *J. Solid State Chem.* **73** 40
[35] Tsvyashchenko A V, Sidorov V A, Petrova A E, Fomicheva L N, Zibrov I P, and Dmitrienko V E 2016 *J. Alloys Compd.* **686** 431
[36] Kamaeva L V, Magnitskaya M V, Suslov A A, Tsvyashchenko A V, and Chtchelkatchev N M 2022 *J. Phys.: Condens. Matter* **34** 424001
[37] Dong X, Zhang B, Ye X, Wei P, Lian L, Sun N, Long Y, Tian S, Wang S, Lei H, and Yu R 2025 *Chin. Phys. B* **34** 088101
[38] Xu S, Zhou L, Wang X Y, Wang H, Lin J F, Zeng X Y, Cheng P, Weng H, and Xia T L 2020 *Chin. Phys. Lett.* **37** 107504
[39] Tsvyashchenko A, Sidorov V, Fomicheva L, Krasnorussky V, Sadykov R, Thompson J, Gofryk K, Ronning F, and Ivanov V 2012 *SSP* **190** 225
[40] DiTusa J F, Zhang S B, Yamaura K, Xiong Y, Prestigiacomo J C, Fulfer B W, Adams P W, Brickson M I, Browne D A, Capan C, Fisk Z, and Chan J Y 2014 *Phys. Rev. B* **90** 144404
[41] Baek S H, Sidorov V A, Nikolaev A V, Klimczuk T, Ronning F, and Tsvyashchenko A V 2022 *Phys. Rev. B* **105** 165132
[42] Lee P A and Ramakrishnan T V 1985 *Rev. Mod. Phys.* **57** 287
[43] Kondo J 1964 *Progr. Theoret. Phys.* **32** 37
[44] Wang Y, Xie C, Li J, Du Z, Cao L, Han Y, Zu L, Zhang H, Zhu H, Zhang X, Xiong Y, and Zhao W 2021 *Phys. Rev. B* **103** 174418
[45] Xu X, Wang X, Cochran T A, Sanchez D S, Chang G, Belopolski I, Wang G, Liu Y, Tien H J, Gui X, Xie W, Hasan M Z, Chang T R, and Jia S 2019 *Phys. Rev. B* **100** 045104
[46] Wu D S, Mi Z Y, Li Y J, Wu W, Li P L, Song Y T, Liu G T, Li G, and Luo J L 2019 *Chin. Phys. Lett.* **36** 077102
[47] Stishov S M, Petrova A E, Sidorov V A, and Menzel D 2012 *Phys. Rev. B* **86** 064433
[48] Magnitskaya M, Chtchelkatchev N, Tsvyashchenko A, Salamatin D, Lepeshkin S, Fomicheva L, and Budzynski M 2019 *J. Magn. Magn. Mater.* **470** 127
[49] Kanazawa N, Onose Y, Shiomi Y, Ishiwata S, and Tokura Y 2012 *Appl. Phys. Lett.* **100** 093902
[50] Basak S, Kobiałka A, Sternik M, Łażewski J, Jochym P T, Oleś A M, Piekarz P, and Ptok A 2024 *Comput. Mater. Sci.* **244** 113149
[51] Petrova A E, Krasnorussky V N, Shikov A A, Yuhasz W M, Lograsso T A, Lashley J C, and Stishov S M 2010 *Phys. Rev. B* **82** 155124
[52] Xu S, Zhou L, Wang H, Wang X Y, Su Y, Cheng P, Weng H, and Xia T L 2019 *Phys. Rev. B* **100** 245146